Online-Journals.org

iJOE International Journal of Online and Biomedical Engineering

iJOE | eISSN: 2626-8493 | Vol. 21 No. 3 (2025) | OPEN ACCESS

https://doi.org/10.3991/ijoe.v21i03.52189

PAPER

Efficient and Parallel Medical Image Segmentation Model (EPSM) Based on Brink-MCET Using Heterogeneous Distributions

Ibrahim N. Dhaini(✉), Ali El-Zaart, Soha Rawas

Department of Mathematics and Computer Science, Faculty of Science, Beirut Arab University, Beirut, Lebanon

ind301@student.bau.edu.lb

ABSTRACT

Medical image segmentation is becoming increasingly popular in the field of image analysis. In computer vision, medical image segmentation is a challenging task but is crucial for identifying and analyzing diseased areas in the body. It is especially crucial for detecting conditions such as brain tumors, skin cancer, and other serious illnesses. This paper presents a novel thresholding technique based on minimum cross-entropy thresholding (MCET), specifically designed for precise segmentation of dermoscopy images. The suggested bimodal technique was evaluated using three benchmark datasets from PH2, HAM10000, and ISIC 2017. To determine the MCET of each input image, three different combinations of statistical distributions—Gaussian, Gamma, and Lognormal—were employed. To further raise the effectiveness of the effective and parallel segmentation model (EPSM) model, a novel parallel boosting segmentation technique was created and applied. By comparing the proposed image segmentation method's output with that of the Entropy-Li approach, its effectiveness was assessed. Both supervised and unsupervised evaluation methods were used. Based on the obtained outcomes, it can be inferred that the EPSM segmentation model is a reliable, accurate, and consistent method with outstanding performance characteristics.

KEYWORDS

medical image segmentation, minimum cross-entropy thresholding (MCET), hybrid distributions, parallel computing

1 INTRODUCTION

Image analysis is the process of analyzing and interpreting raw image data in order to offer a solution for an imaging task. An image is considered to have undergone analysis when the data in this image is assessed [1]. Image enhancement, image segmentation, region extraction, and pattern classification are further

Dhaini, I.N., El-Zaart, A., Rawas, S. (2025). Efficient and Parallel Medical Image Segmentation Model (EPSM) Based on Brink-MCET Using Heterogeneous Distributions. *International Journal of Online and Biomedical Engineering (iJOE)*, 21(3), pp. 142–164. https://doi.org/10.3991/ijoe.v21i03.52189

Article submitted 2024-09-11. Revision uploaded 2024-12-17. Final acceptance 2024-12-18.

techniques that fall under the umbrella of image analysis. A traditional topic of study in computer vision, image segmentation has recently garnered attention in the realm of image analysis. There exist several real-world uses for image segmentation, including medical image analysis, object detection and recognition, surveillance, satellite imaging, traffic signal systems, etc. Medical image segmentation, which is a significant challenge in computer vision, offers essential details about the sick area that may necessitate in-depth analysis [2]. Additionally, it gives professionals the data they need to diagnose, monitor, or choose the best course of action for a patient's condition.

The methods used for segmenting images may fall into four major classes: thresholding-based, region-based, edge or boundary-based, and hybrid methods [3]. Despite being the most popular approach, deep learning-based image segmentation is not without its well-known drawbacks [4]. Under certain conditions, deep learning might not be practical because of the high processing overhead, lengthy training times, and intricate architecture. In contrast, thresholding approaches are the most often used techniques for categorizing image pixels into two or more classes due to their simplicity, stability, good computational speeds, and ease of implementation [5]. The thresholding strategy's primary goal is to select the optimal threshold depending on how intensely the object and background of the image are distributed. Based on the characteristics of every pixel, the thresholding techniques can also be divided into global or local. Global techniques use a global single threshold on all the pixels in an image to label whether they belong to the object or the background. [6]. In contrast, local thresholding methods determine each pixel's threshold based on the characteristics of its neighbors [6]. The computational expenses involved in determining the global thresholding are lower than those of determining the local thresholding [7]. Entropy-based thresholding methods with relevant variation approaches are widely employed as a form of global thresholding. Entropy-based thresholding techniques rely on the information content of the image histogram to determine the threshold that divides a given image into two classes. Pun [8] was the first to employ entropy for calculating the threshold, relying on the probability distribution of the histogram of a specific image. Later, Kapur [9] enhanced Pun's work and developed a new approach called maximum entropy thresholding. Li and Lee [5] suggested that the cross-entropy between a particular image and the segmented one be minimized to choose the best threshold. Subsequently, Brink and Pendock [10] suggested an enhancement of Li's work while still using minimum cross entropy. Minimum cross-entropy thresholding (MCET), one of many entropy-based approaches, has drawn a lot of interest in the field of image segmentation [11]. Finding the distribution or combination of distributions that best represents the data in the image histogram is one of the primary aspects that may have an impact on the MCET outcomes [12].

This paper's main objective is to provide an effective and parallel segmentation model (EPSM) based on Entropy-Brink to determine the best threshold for distinguishing an image's foreground from background in dermoscopy images. The suggested model is evaluated using PH2, HAM10000, and ISIC 2017, three independent benchmark datasets. To calculate the MCET of each input image, three different combinations of the Gaussian, Gamma, and Lognormal statistical distributions were used. The proposed model was evaluated using unsupervised metrics, and the effectiveness of the suggested threshold for segmentation was determined by comparing the output images to the ground truth images using supervised metrics.

This paper addresses the following:

1. Developing an EPSM model using MCET and a blend of thresholding techniques, including Gaussian, Gamma, and Lognormal, and evaluating its performance on dermoscopy images.
2. Utilizing a mathematical model to improve the segmentation outcomes obtained with the EPSM approach.
3. Developing and putting into action a new concurrent boosting segmentation algorithm to enhance the performance of the EPSM approach.

The remainder of the paper is divided into the following sections: A summary of the relevant studies is included in Section 2. In Section 3, under the topic of Materials and Methods, we covered the following: cross-entropy thresholding, minimum cross-entropy thresholding, and probabilistic distributions. We presented the EPSM-Brink formulation and demonstrated how the EPSM approach is applied to address the segmentation problem. Additionally, this section includes a discussion of the study's performance metrics and the use of parallel processing to enhance the efficiency of the EPSM-Brink technique. Sections 4 and 5 provide a conclusion and an evaluation of the EPSM-Brink technique, as well as a discussion of possible directions for future research in the area of image segmentation.

2 RELATED WORK

Due to the increased demand for automated image analysis across a variety of disciplines, especially medical diagnostics, many articles in recent years have focused on developing efficient and trustworthy image segmentation methods. This part of the paper reviews the pertinent research on image segmentation and thresholding methods, which serve as the foundation for the suggested approach.

A model for segmenting brain tumors from brain MRIs that uses a combination of thresholding and morphological techniques was recently introduced by Nyo and colleagues [13]. They used Otsu's thresholding approach to define the tumor location inside the MRI scans by first converting the images to grayscale and then removing noise. A morphological procedure is used to fine-tune and precisely identify the tumor locations in the final step. Wang et al. [14] suggested a multi-threshold model based on the Otsu segmentation approach to segment medical images. Breast cancer photos in both color and grayscale were used to test the proposed methodology. The authors paired the proposed strategy with the metaheuristic-augmented Dandelion Optimization method to lengthen the segmentation computation time. On dermoscopy lesion images, Ramya et al. [15] recommended using image segmentation to separate the skin lesion from the surrounding tissue. Initially, discrete wavelet transform (DWT) is applied to each color component after separating the image's color components. The skin lesion region is afterward separated from the backdrop using Otsu and histogram-based thresholding. Jumiawi and El-Zaart [16] presented an image segmentation approach for images with right-skewed intensity histograms that makes use of the Otsu method. They chose to compute the between-class variance for these specific image types using the lognormal distribution rather than the Gaussian distribution. Their suggested model's main objective is to solve the drawbacks of asymmetric distributions, particularly for images with right-skewed intensity levels.

In their 1993 publication, Li and Lee introduced the MCET technique [5]. In this paper, the authors proposed a new thresholding approach based on the concept of cross-entropy. Subsequently, Brink and Pendock [10] developed a brand-new method for equalizing histograms that involves minimizing the cross-entropy between the intended histogram and the original image histogram, subject to a pixel count restriction. Using a combination of Poisson distributions to represent the image histogram, Pal [17] suggested a new MCET method to determine the optimal threshold. Zreika [18, 19] introduced two thresholding techniques that are based on the MCET method that compute the ideal threshold for separating the foreground and background of an image using the Entropy-Pal criterion. The image histogram was modeled in the first research using Gaussian and Poisson distributions and in the second study using Gaussian and lognormal distributions. Rawas et al. [20] implemented a method known as HCET-G2 for segmenting dermoscopic skin lesions. It uses a hybrid cross-entropy thresholding approach that utilizes both Gaussian and Gamma distributions. Rawas et al. [12] proposed a new hybrid segmentation method built by integrating Gaussian, gamma, and lognormal distributions based on MCET. Jumiawi et al. [21] used the MCET technique to create a new model for segmenting images. This technique handles images with either left- or right-skewed histograms by using Gumbel's distribution. The authors specifically used Gumbel's distribution to compute the mean values for the object and background in these skewed-histogram images.

Deep learning-based methods for medical image analysis have become popular in recent years. To increase the U-Net model's learning effectiveness, Farahani et al. [22] applied the model to datasets of retinal and skin lesions while introducing parameter changes. The authors of [23] also suggested a new deep learning segmentation framework that combines the U-Net architecture and the level set model.

To increase the computing efficiency of sequential image segmentation, a number of parallel strategies have been proposed in recent years. Rahimi et al. [24] proposed a parallel algorithm for image segmentation based on the Fuzzy C-Means (FCM) clustering algorithm. M. Al-Ayyoub et al. [25] presented a parallel implementation of the Fuzzy C-Means (FCM) algorithm for medical image segmentation using Graphics Processing Units. Prahara et al. [26] suggested a parallelized approach to implement three adaptive image thresholding methods, namely Otsu, ISODATA, and minimum cross-entropy, by utilizing GPUs. M. Nishat Akhtar et al. [27] proposed a parallel image segmentation algorithm that leverages the MapReduce framework and uses a modified version of the k-means clustering algorithm to segment the image into regions of similar intensity values.

In the aforementioned methods, various methods were put out and evaluated on various datasets. Dermoscopy images can be segmented using some of these methods; skin images can be segmented using others, and breast cancer images can be segmented using still others. The described MCET-based methodologies range from utilizing homogeneous distribution to compute the mean values of the object and background to employing two distributions to handle the segmentation strategy. Jumiawi et al.'s study [21] recommended using Gumbel's distribution to handle particular instances of photos with skewed histograms. In the other piece of work by Jumiawi et al. [16], the suggested method explicitly targeted images with right-skewed histograms by applying lognormal distribution. Other research offered a multi-level threshold strategy for segmenting images into more than two separate parts. While some studies can only be applied to grayscale images, others can be

applied to both color and grayscale photographs. Except for the study carried out by Rawas et al. [12], none of the aforementioned works utilized a combination of three statistical distributions simultaneously to determine the ideal threshold for segmenting an image into foreground and background. In order to determine the threshold, this work included three benchmark distributions (Gamma, Gaussian, and Lognormal); however, the entropy of Brink was employed in place of Rawas et al.'s Entropy of Li.

3 MATERIALS AND METHODS

3.1 Materials

Experiments are carried out in this section to assess the feasibility of the proposed EPSM model. All experiments are carried out using the MATLAB R2020a toolbox on an Intel(R) Core (TM) i7-1065G7 @ 1.30GHz computer with 8 GB RAM. In addition, this central processing unit (CPU) generation is distinguished by having four total cores with eight threads. Several MATLAB routines that make use of the parallel computing toolbox to parallelize the model are used to generate a multi-threaded version of it.

Datasets. Three different benchmark datasets were used to evaluate the proposed EPSM-MCET segmentation model, allowing for an unbiased evaluation of the model's accuracy and efficacy. The used datasets' specifications are shown in Table 1.

PH2: The PH2 dataset was created to enable comparative analysis of dermoscopic image classification and segmentation algorithms, and it was acquired from the Dermatology Service of Hospital Pedro Hispano in Matosinhos, Portugal [28]. The dataset includes 200 dermoscopic pictures of pigmented skin lesions, and expert dermatologists have annotated each image with ground-truth segmentation masks for the lesions.

ISIC 2017: 2017 saw the release of a dataset from the International Skin Imaging Collaboration (ISIC) that included 2000 dermatoscopy images for the training set, 150 images for the validation set, and 600 images for the ultimate test set [29]. A number of skin cancer specialists made the "ground truth" diagnosis for each image in the collection. For each image in the collection, clinical details such as the patient's age and sex are also included.

HAM10000: The HAM10000 [30] dataset consists of 10,015 excellent dermatoscopic photos of skin lesions that were obtained from various populations and by utilizing various methods. For usage in machine learning applications and comparisons with human experts, the images are made available to the public through the ISIC repository.

Table 1. Dataset specifications

Dataset	Dataset Classification	Dataset Images Count	Annotated
PH2	Dermatoscopic	200	Yes
ISIC 2017	Dermatoscopic	2000	Yes
HAM10000	Dermatoscopic	10,015	Yes

3.2 Image segmentation and thresholding

The image segmentation objective is to divide the image into two segments, one representing the foreground object(s) and the other representing the background [5]. The image segmentation process is challenging, especially when dealing with images that have a complex structure or contain multiple objects, as it requires knowledge of both low-level features, such as color and texture, and high-level features, such as shape, size, or category of objects [31]. Image thresholding is based on the simple idea of dividing an image into two regions or segments based on a threshold value applied to a certain feature, such as pixel intensity or color [12]. Even though many thresholding methods have been put forth over the years, the entropy-based thresholding method is still the most widely used [32]. The thresholding segmentation technique applies to both bimodal and multimodal images.

In bimodal thresholding, the image has two peaks in the histogram, representing foreground and background pixels. The threshold value is selected at the valley between the two peaks, and pixels with intensity values above the threshold are assigned to one segment while those below it are assigned to the other [11]. Let t^* be the optimal threshold that divides the two distinct regions A and B, where A and B are segment 1 and segment 2, respectively, and $h(x)$ be the histogram of an image f such that:

$$g(x,y)=\begin{cases}0, & f(x,y)<t^*\\ 255, & f(x,y)\geq t^*\end{cases} \tag{1}$$

An image's pixel intensity is denoted by the notation $g(x, y)$, while t^* is a gray level value within the range of the image histogram [0–255]; see Figure 1. Multimodal thresholding, which is outside the purview of this study, is employed when an image has numerous regions with various intensities [12].

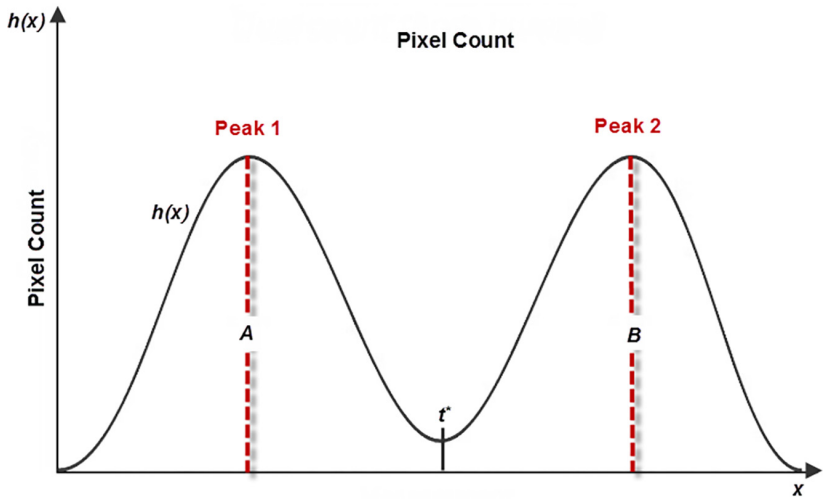

Fig. 1. Bimodal image histogram

Cross-entropy thresholding. In 1968, Kullback [33] came up with a statistical measure called Kullback-Leibler divergence, which measures how different two probability distributions are from one another. It gauges the amount of information lost when attempting to approximate the other probability distribution using the first one. Given two probability distributions P and Q defined on the same set such

that $P = \{P_1, P_2, ..., P_N\}$ and $Q = \{Q_1, Q_2, ..., Q_N\}$, the cross-entropy between P and Q is defined as follows:

$$D(P,Q) = \sum_{k=1}^{N} p_k . \log_2 \frac{p_k}{q_k} \tag{2}$$

Where, N refers to the number of values in the distribution, p_k represents the probability of event k according to the probability distribution P, and q_k signifies the probability of event k according to the probability distribution Q.

Brink and Pendock [10] observed that Kullback-Leibler divergence is not symmetric, meaning that $D(P, Q)$ is not equal to $D(Q, P)$, and imposed additional criteria to the equation:

$$D(P,Q) = \sum_{k=1}^{N} p_k . \log_2 \frac{p_k}{q_k} + \sum_{k=1}^{N} q_k . \log_2 \frac{q_k}{p_k} \tag{3}$$

Hence, the cross-entropy between the original image denoted by $I(x, y)$ and the thresholded image denoted by $I_t(x, y)$ is defined by the Entropy-Brink algorithm as follows:

$$\begin{aligned} D(I,I_t) = &\sum_{i=0}^{t} h(i) \left[i \times \log\left(\frac{i}{\mu_1(t)} \right) + \mu_1(t) \times \log\left(\frac{\mu_1(t)}{i} \right) \right] \\ &+ \sum_{i=t+1}^{L} h(i) \left[i \times \log\left(\frac{i}{\mu_2(t)} \right) + \mu_2(t) \times \log\left(\frac{\mu_2(t)}{i} \right) \right] \end{aligned} \tag{4}$$

The equation uses $\mu_1(t)$ and $\mu_2(t)$ to illustrate the respective means of the first and second modes. Additionally, $h(i)$ represents the image's histogram, where i ranges from 1 to L, the maximum grey level.

Minimum cross-entropy thresholding. In 1992, Li and Lee [5] proposed the MCET method and derived the optimal threshold t^* by minimizing the cross-entropy using the formula as follows:

$$t^* = \arg\min_t (D(I,I_t)) = \arg\min_t (D(t)) \tag{5}$$

The equation that minimizes the cross-entropy between the main image and the thresholded one using the Entropy-Brink algorithm can be redefined in the following manner:

$$\begin{aligned} D(t) = &\sum_{i=0}^{L} i.h(i).\log i + \sum_{i=0}^{t} \mu_1 .h(i).\log \mu_1 - \sum_{i=0}^{t} \mu_1 .h(i).\log i - \sum_{i=0}^{t} i.h(i).\log \mu_1 \\ &+ \sum_{i=t}^{L} \mu_2 .h(i).\log \mu_2 - \sum_{i=t}^{L} \mu_2 .h(i).\log i - \sum_{i=t}^{L} i.h(i).\log \mu_2 \end{aligned} \tag{6}$$

As the first term in the objective function is constant for the image, it can be expressed as:

$$\begin{aligned} D(t) = &\sum_{i=0}^{t} \mu_1 .h(i).\log \mu_1 - \sum_{i=0}^{t} \mu_1 .h(i).\log i - \sum_{i=0}^{t} i.h(i).\log \mu_1 + \sum_{i=t}^{L} \mu_2 .h(i).\log \mu_2 \\ &- \sum_{i=t}^{L} \mu_2 .h(i).\log i - \sum_{i=t}^{L} i.h(i).\log \mu_2 \end{aligned} \tag{7}$$

Probabilistic distributions. The selection of the optimal threshold for image segmentation is contingent upon identifying the distribution type that characterizes the pixels within the image segment [12]. Such a distribution can be an integration between symmetric and non-symmetric distributions. This paper utilizes Gaussian, Gamma, and Lognormal distributions to identify the most suitable threshold for a given image.

Gaussian distribution. The probability density function of the Gaussian distribution is represented in the following equation [19]:

$$f(x,\mu,\sigma)=\frac{1}{\sigma\sqrt{2\pi}}e^{\left(-\frac{1}{2}\left(\frac{x-\mu}{\sigma}\right)^2\right)} \tag{8}$$

In this context, x represents the intensity level of a pixel, σ denotes the standard deviation, and μ represents the mean. The means $\mu_1(t)$ and $\mu_2(t)$ of the two segments can be inferred from the two Gaussian distributions in image segmentation if it is assumed that the pixel values in the image follow a Gaussian distribution [34]:

$$\mu_{11}(t)=\mu_1(t)=\frac{\sum_{i=0}^{t-1} i.h(i)}{\sum_{i=0}^{t-1} h(i)} \tag{9}$$

$$\mu_{21}(t)=\mu_2(t)=\frac{\sum_{i=t}^{L} i.h(i)}{\sum_{i=t}^{L} h(i)} \tag{10}$$

L represents the image's gray levels, while h denotes the image's histogram. The symbol t represents the computed threshold that segregates the image into two distinct sections, and μ refers to the distribution mean.

Gamma distribution. The definition of the function of the Gamma distribution is given as follows [19]:

$$f(x,\mu,N)=\frac{2q}{\mu}\frac{N^N}{\Gamma(N)}\left(\frac{qx}{\mu}\right)^{2N-1}e^{-N\left(\frac{qx}{\mu}\right)^2} \tag{11}$$

where $q=\frac{\Gamma(N+0.5)}{\sqrt{N}\ .\Gamma(N)}$, N is the shape of the distribution.

When dealing with image segmentation and assuming that the image is made up of two Gamma distributions representing the background and object regions, respectively, the means of these two segments can be estimated. Specifically, the means $\mu_1(t)$ and $\mu_2(t)$ can be estimated using the following equations [35]:

$$\mu_{12}(t)=\mu_1(t)=\sqrt{\frac{\sum_{i=0}^{t-1} h(i).i^2.q^2}{\sum_{i=0}^{t-1} h(i)}} \tag{12}$$

$$\mu_{22}(t)=\mu_2(t)=\sqrt{\frac{\sum_{i=t}^{L} h(i).i^2.q^2}{\sum_{i=t}^{L} h(i)}} \tag{13}$$

Lognormal distribution. The following is a definition of the lognormal distribution's function [19]:

$$f(x,\mu,\sigma) = \frac{1}{x\sigma\sqrt{2\pi}} e^{-\frac{1}{2}\left(\frac{\ln x-\mu}{\sigma}\right)^2} \tag{14}$$

As a result, if the image's data are presumed to follow a lognormal distribution, $\mu_1(t)$ and $\mu_2(t)$ can be estimated using two lognormal distributions as shown below [36]:

$$\mu_{13}(t) = \mu_1(t) = \frac{\sum_{i=0}^{t-1} \log i.h(i)}{\sum_{i=0}^{t-1} h(i)} \tag{15}$$

$$\mu_{23}(t) = \mu_2(t) = \frac{\sum_{i=t}^{L} \log i.h(i)}{\sum_{i=t}^{L} h(i)} \tag{16}$$

3.3 EPSM-brink formulation

This part provides a generic structure for modeling the EPSM that, by locating the best distributions that make up the segmented image's histogram, produces an accurate segmentation model. Therefore, the purpose of selecting the best distributions is to determine the optimal threshold value (t^*).

Modeling the thresholding problem. Finding the sort of distribution that minimizes the MCET and results in the optimal threshold value (t^*) for image segmentation transforms the image segmentation problem into an NP-hard optimization problem [12]. In essence, the goal is to identify the threshold value that minimizes the cross-entropy criterion, leading to an effective segmentation of the image.

$$Minimize\ (t^*) \tag{17}$$

In addition, accurate segmentation emphasizes optimizing both unsupervised metrics and supervised metrics.

The proposed EPSM approach. This paper proposes an EPSM-based MCET technique for heterogeneous thresholding with Gaussian, Gamma, and Lognormal distributions. The proposed approach is described in detail as follows:

To minimize the t^* thresholding value, an image $I(x, y)$ is formed of two regions, each with distinct statistical properties. Each region can be represented by a different probability distribution, such as Gaussian, Gamma, or Lognormal. So, to *minimize* (t^*) and get the best segmentation performance, equations 9, 10, 12, 13, 15, and 16 can be utilized to estimate $\mu_1(t)$ and $\mu_2(t)$ from two different distributions, depending on the assessed region. The two cases below result from this mixture model:

$$h(x) = Pr_1 * distribution_1(x,\mu_1(t)) + Pr_2 * distribution_2(x,\mu_2(t)) \tag{18}$$

such that 1) $distribution_1(x, \mu_1(t))$ is the first distribution of the first region and can be Gaussian, lognormal, or gamma; and 2) $distribution_2(x, \mu_2(t))$ is the second distribution for the second region and can be Gaussian, lognormal, or gamma. Taking into consideration that Pr_1 and Pr_2 are two prior probabilities, $Pr_1 + Pr_2 = 1$. Pr_1 and Pr_2 are modified using an iterative process. Based on the current threshold and the pixel intensities that fall into each region, Pr_1 and Pr_2 are changed at each iteration. The key phases of the suggested approach are shown in Figure 2.

3.4 Performance measure

For a variety of datasets, the suggested hybrid MCET method based on the Brink approach was used, and the outcomes of the image segmentation on different datasets were then compared and evaluated with the results of the precise and parallel segmentation model (PPSM) and the deep learning model U-Net. As stated in Section "Modeling the thresholding problem", precise segmentation aims to maximize performance metrics to increase the accuracy indicator. Both supervised and unsupervised methods were employed to address this problem.

$$Maximize\ (S,U) \tag{19}$$

In Equation 19, the letter S is used to denote the supervised evaluation metrics, which include *JI, DI,* and *F-score*. On the other hand, the letter U is used for unsupervised evaluation metrics, such as $U(t)$ and *RC*. Every evaluation metric, both supervised and unsupervised, has a value between 0 and 1, with values closer to 0 indicating low quality and closer to 1 indicating better segmentation results. The optimal threshold value (t^*) can range between 0 and 255.

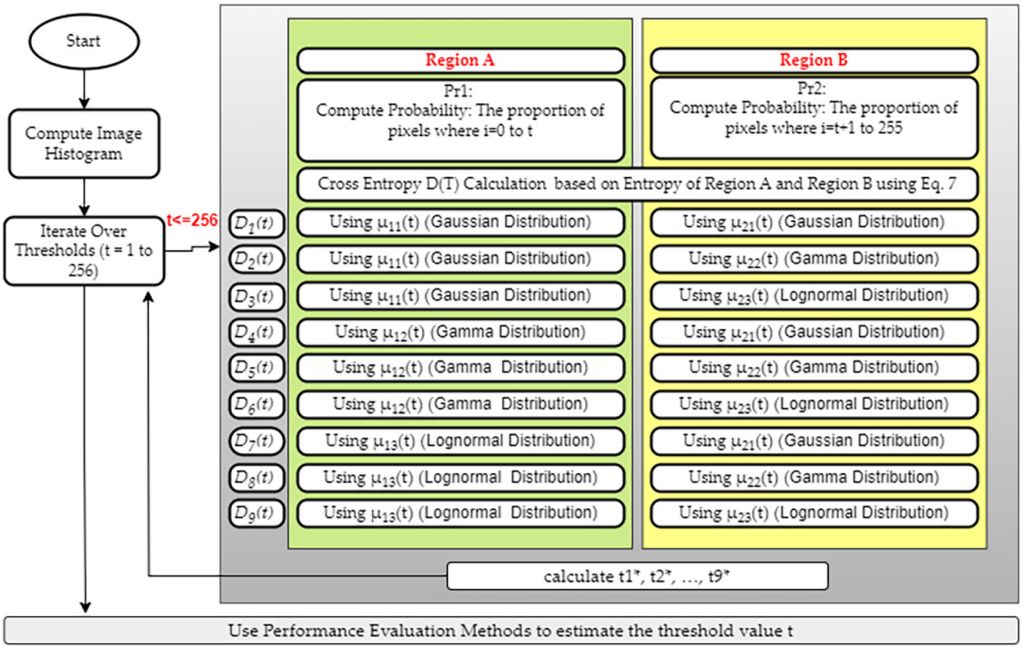

Fig. 2. The proposed EPSM approach

Supervised evaluation metrics require annotated images for accurate evaluation, whereas unsupervised evaluation metrics can be used in the absence of annotated images. Therefore, if annotated images are not available, only the unsupervised metrics will be used to assess the effectiveness of the segmentation findings.

Unsupervised evaluation measures. Without the use of a reference image, unsupervised evaluation techniques, sometimes referred to as stand-alone evaluation methods [37], evaluate the effectiveness of a segmented image by contrasting it with a list of desired features of segmented images as seen by people. Uniformity measure and region contrast measure are examples of these unsupervised evaluation measures.

Uniformity measure: $U(t)$ is a quantitative metric used to evaluate the homogeneity of pixels within a region of an image [38]. For a criterion threshold t, $U(t)$ is calculated using the following equation:

$$U(t) = 1 - \frac{Q_1^2(t) + Q_2^2(t)}{C} \tag{20}$$

where $Q_1^2(t)$ and $Q_2^2(t)$ represent the variance of segment A and segment B, respectively, as seen in Figure 1. $Q_1^2(t)$ and $Q_2^2(t)$ are calculated using the following equations:

$$Q_1^2(t) = \frac{\sum_{i=0}^{t-1} (i - \mu_{1(t)})^2 * h(i)}{\sum_{i=0}^{t-1} h(i)} \tag{21}$$

$$Q_2^2(t) = \frac{\sum_{i=t}^{L} (i - \mu_{2(t)})^2 * h(i)}{\sum_{i=t}^{L} h(i)} \tag{22}$$

where L stands for the highest possible grey level, 255, and $h(i)$ indicates the image's histogram. Equations [9–10] are used to determine the mean of the object, which is denoted by $\mu_1(t)$, and the mean of the background, which is denoted by $\mu_2(t)$. C is a normalization factor calculated using the following equation:

$$C = \frac{(g_{max} - g_{min})^2}{2} \tag{23}$$

The values of g_{min} and g_{max} must both fall within the range [0–255], where g_{min} indicates the minimum gray level value and g_{max} represents the highest possible gray level value.

Region contrast: The dissimilarity between two segments of an image is measured quantitatively using the inter-region contrast. It serves as a performance indicator for image segmentation techniques by calculating the difference in mean pixel values between the object segment and the background segment [37]. The RC is computed using the following equation:

$$RC(t) = \frac{|\mu_1(t) - \mu_2(t)|}{\mu_1(t) + \mu_2(t)} \tag{24}$$

where $\mu_1(t)$ and $\mu_2(t)$ are calculated using equations [9, 10], respectively.

It should be noted that, like the $U(t)$ measure, the value of RC spans between [0, 1], with 0 denoting poor segmentation performance and 1 denoting ideal segmentation performance, respectively, for a specific threshold value t.

Supervised evaluation measures. Supervised evaluation methods, also called relative evaluation methods [37], are pixel-based evaluation methods to test segmentation algorithms by comparing the resulting segmented image to a manually segmented reference image, which is commonly known as a ground truth. The EPSM model was evaluated using performance metrics that are considered supervised evaluation measures, including the Jaccard Index (*JI*), Dice Index (*DI*), and *F-score*. These measures are computed by utilizing the counts of true positives (*TP*), false positives (*FP*), true negatives (*TN*), and false negatives (*FN*) generated by the algorithm's segmentation of the image.

$$JI = \frac{TP}{TP + FP + FN} \tag{25}$$

$$DI = \frac{2TP}{2TP + FP + FN} \tag{26}$$

$$F\text{-}score = 2 * \frac{precision * recall}{precision + recall} \tag{27}$$

True positive, *TN*, *FP*, and *FN*, which are used in the equations above, are further defined as [39]:

- True positive denotes the count of pixels that were correctly identified as belonging to the object of interest in both the segmented image and the ground truth image.
- True negative stands for the count of pixels in both the segmented image and the ground truth image that are correctly identified as not being part of the item of interest.
- False positives represent the count of pixels in the segmented image that are mistakenly assigned to the object of interest but are not in the ground truth image.
- False negatives stand for the count of pixels that were mistakenly identified in the segmented image as not being part of the object of interest, despite being present in the ground truth image.

The range of values for these metrics is from 0 to 1, with a score of 0 indicating poor segmentation performance and a score of 1 indicating ideal segmentation performance. In other words, the closer the score is to one, the segmentation outcome is considered superior.

3.5 Solving the EPSM approach

This part presents the EPSM approach that computes the optimal threshold (t*) value to guarantee a precise separation of the object from its background in a given input image.

EPSM approach. The pseudocode in Algorithm 1 determines the MCET value for the input image "*I*." By repeatedly testing different threshold values, "t," and calculating the cross-entropy value between two segments of pixel intensities, one below and one above the threshold value, the ideal threshold value, "t*," is computed. The code first reads the input image (line 1) and calculates the image's histogram (h(x) of the image $I(x,y)$) (line 2). Next, using a combination of distributions, it calculates the mean value 1 and mean value 2 for the background and object intensity zones, respectively, for each potential threshold value "t" (lines 4 to 6). The entropy of the background intensity zone and that of the object intensity region are then calculated. The function then uses the combination of distributions to determine the cross-entropy value for the current threshold "t" (lines 7 and 8). The unsupervised measurements are calculated following the loop (line 11). The supervised metrics are computed if ground truth images are present with the dataset (line 12). In order to find the appropriate threshold and return it, the last step is to maximize the supervised and unsupervised outcomes (lines 13–16).

Algorithm 1: EPSM Algorithm

Parameter: $I(x, y)$ % The main input image
Outcome: t* % The optimal threshold
Steps:

1. Read image $I(x, y)$
2. Compute the input image's histogram h(i), where i=0, …., 255
3. while i = 1 to 255 do
4. Compute $\mu_{11}(i)$ and $\mu_{21}(i)$ using Equations (9-10)
5. Compute $\mu_{12}(i)$ and $\mu_{22}(i)$ using Equations (12-13)
6. Compute $\mu_{13}(i)$ and $\mu_{23}(i)$ using Equations (15-16)
7. Using Equation 7,
   Compute cross-entropy $D_1(t)$ *using* $\mu_{11}(i)$ *for class* 1 *and* $\mu_{21}(i)$ *for class* 2
   Compute cross-entropy $D_2(t)$ *using* $\mu_{11}(i)$ *for class* 1 *and* $\mu_{22}(i)$ *for class* 2
   Compute cross-entropy $D_3(t)$ *using* $\mu_{11}(i)$ *for class* 1 *and* $\mu_{23}(i)$ *for class* 2
   Compute cross-entropy $D_4(t)$ *using* $\mu_{12}(i)$ *for class* 1 *and* $\mu_{22}(i)$ *for class* 2
   Compute cross-entropy $D_5(t)$ *using* $\mu_{12}(i)$ *for class* 1 *and* $\mu_{21}(i)$ *for class* 2
   Compute cross-entropy $D_6(t)$ *using* $\mu_{12}(i)$ *for class* 1 *and* $\mu_{23}(i)$ *for class* 2
   Compute cross-entropy $D_7(t)$ *using* $\mu_{13}(i)$ *for class* 1 *and* $\mu_{23}(i)$ *for class* 2
   Compute cross-entropy $D_8(t)$ *using* $\mu_{13}(i)$ *for class* 1 *and* $\mu_{21}(i)$ *for class* 2
   Compute cross-entropy $D_9(t)$ *using* $\mu_{13}(i)$ *for class* 1 *and* $\mu_{22}(i)$ *for class* 2
8. Using the various distribution combinations, calculate $t_1^*, t_2^*, \ldots, t_9^*$
   ex: if $D_k(t) <$ min-value$_{-k}$ % k = 1, 2, 3, 4, 5, 6, 7, 8, 9 respectively
   min-value$_{-k} = D_k(t)$
   $t_k^* = j$
   end
9. i = i + 1
10. end % end loop
11. Compute the unsupervised measures $U(t_1^*), U(t_2^*), \ldots, U(t_9^*)$
    % using equations 20 and 24
12. Compute the supervised measures if the ground truth images are available
    % using equations 25, 26, and 27
    ex: if GT exists
    $S(t_1^*), S(t_2^*), \ldots, S(t_9^*)$
    end
13. best(t) = Maximum$\left(\left\{S(t_1^*), U(t_1^*)\right\}, \left\{S(t_2^*), U(t_2^*)\right\}, \ldots, \left\{S(t_9^*), U(t_9^*)\right\}\right)$
14. t* = t
15. end if
16. return t*

3.6 Parallel processing

The MCET approach has to analyze each potential threshold value t iteratively to find the ideal threshold value t^* by minimizing cross entropy. This process may require a lot of computer power, particularly for large or numerous small images. The procedure can be sped up while maintaining the method's effectiveness by properly utilizing parallel processing techniques [12].

By manipulation of its fundamental parallelism, parallel processing technology has been leveraged to accelerate application performance [40]. This part aims to utilize this technology and enhance the performance of the EPSM method using parallel CPUs and GPUs. To get around the processing time issue, the suggested EPSM method has been parallelized to harness all the computational resources available.

EPSM method with parallel processing techniques. The stages that explain how to apply parallel processing techniques for obtaining the MCET on a collection

of images are shown in Figure 3, and the following points provide further details of the process:

1. Minimum cross-entropy thresholding for each image: To process numerous images simultaneously and find the ideal threshold value for each one, the process of determining the optimal threshold t* for a group of images can be divided into a job and carried out in parallel mode.
2. Calculating the means of the object and background segments using hybrid distributions: Each mean of a particular segment can be calculated using a Gaussian, Gamma, or Lognormal distribution on a specific thread, and the results are collected in an array that can be used by all other code stages.
3. Unsupervised measures: The unsupervised measures can be handled apart from the other tasks.
4. Supervised measures: These measurements can also be computed and handled differently from the other tasks.

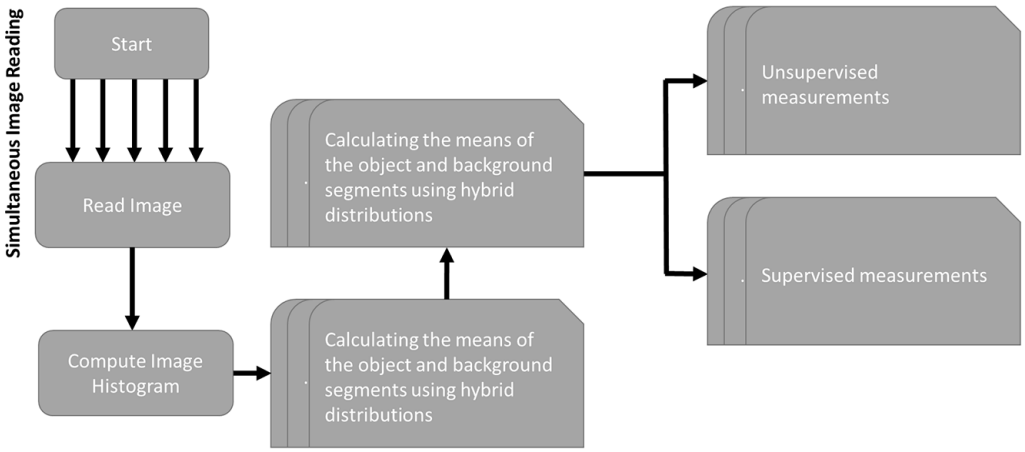

Fig. 3. Structure of the parallelized EPSM approach

4 RESULTS AND DISCUSSION

In this part, various experiments were carried out to evaluate the effectiveness of the EPSM model and to measure the possible speedup achievable by applying the parallel techniques described in the section "EPSM method with parallel processing techniques". The experiments were conducted on three benchmark datasets, namely PH2, HAM10000, and ISIC 2017. Three alternative combinations of the statistical distributions Gaussian, Gamma, and Lognormal were utilized to determine the MCET of each input image. To compare the results of implementing and executing the EPSM model, the PPSM model was also implemented and run. Unsupervised metrics were utilized to assess the proposed model, while supervised metrics were used to contrast the output images with the reference images to see if the suggested threshold results in effective or ineffective segmentation.

Furthermore, the outcomes of applying and executing the EPSM model on samples from the three mentioned datasets were compared with the results obtained from running the same samples using the deep learning model known as U-Net.

U-Net, a neural network architecture that was created mainly for image segmentation [41] and is a popular choice for medical image segmentation due to its effectiveness in this domain [42].

The U-Net model was trained using the Adam optimizer. As is suitable for binary classification tasks, a binary cross-entropy loss function was employed for the classification challenge. The Dice loss function, a popular statistic in medical image segmentation [43], was employed for the segmentation challenge.

4.1 Accuracy

For the three-benchmark datasets, Table 2 displays the outcomes of using the suggested model with various statistical distribution combinations. The number of images for each dataset that could be best segmented using a combination of two distributions is shown in that table. The proportion of thresholded images with the best performance is also displayed in a separate column. It was found that 65% of the segmented images were produced utilizing a combination of heterogeneous distributions when the suggested model was applied to the PH2 and ISIC 2017 datasets. A hybrid distribution combination successfully segmented 59.4% of the images in the HAM10000 dataset.

Comparing the outcomes of using the EPSM and PPSM models on the same datasets is made very evident in Table 3. The comparison shows how the suggested model performs better on these datasets than the PPSM model. For instance, in the PH2 dataset, the suggested model outperformed Li's method for segmenting 98% of the images. Li's method, however, produced a better segmentation threshold for 2% of the images. The suggested method outperformed Li's method in 93.6% of the images in the HAM10000 dataset, while Li's method produced better thresholding in only 1% of the images. Both methods produced subpar segmentation for 5.4% of the images. The proposed method outperformed Li's method for 93.8% of the images in the ISIC 2017 dataset. Li's method, however, produced better thresholding for 3.2% of the images. Poor segmentation was produced by both methods for 3% of the images. Figure 4, a clustered column chart, provides an image of these results.

These results, taken together, demonstrate that the proposed EPSM model outperforms the PPSM model on these benchmark datasets.

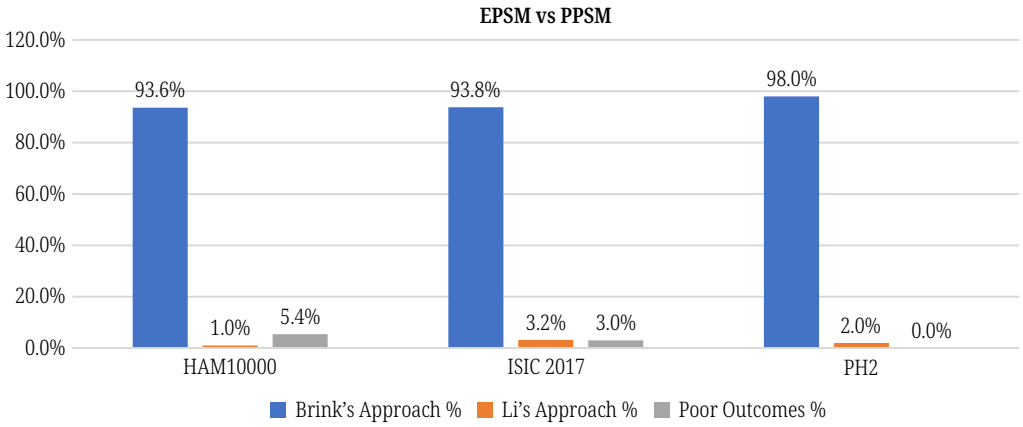

Fig. 4. Chart showing the results of using the PPSM and EPSM techniques on the PH2, ISIC 2017, and HAM10000 datasets

Table 2. Combinations of heterogeneous distributions from the EPSM model

Distributions	PH2		ISIC 2017		HAM10000	
	Number of Optimal Segmented Images	Optimum Performance (%)	Number of Optimal Segmented Images	Optimum Performance (%)	Number of Optimal Segmented Images	Optimum Performance (%)
Gaussian	63	31.5	97	19.4	152	30.4
Gaussian-Gamma	127	63.5	220	44	163	32.6
Gaussian-Lognormal	0	0	1	0.2	1	0.2
Gamma	7	3.5	97	19.4	51	10.2
Gamma-Gaussian	3	1.5	84	16.8	133	26.6
Gamma-Lognormal	0	0	1	0.2	0	0
Lognormal-Gaussian	0	0	0	0	0	0
Lognormal-Gamma	0	0	0	0	0	0
Lognormal-Lognormal	0	0	0	0	0	0
	200	100%	500	100%	500	100%

Table 3. The comparison of applying the EPSM and PPSM on the same datasets

Dataset	Brink's Approach	Li's Approach	Poor Outcomes (0)	Sample Count
HAM10000	468 (93.6%)	5 (1%)	27 (5.4%)	500
ISIC 2017	469 (93.8%)	16 (3.2%)	15 (3%)	500
PH2	196 (98%)	4 (2%)	0 (0%)	200

Examples of the outcomes of using the HAM10000, ISIC 2017, and PH2 datasets with the EPSM and PPSM models are shown in Tables 4, 5, and 6, respectively. Each table shows ten sample images, along with the results of applying Li's method and the suggested model to each image. The optimal distribution combination for both procedures is also given, along with the segmentation threshold result. Also, the performance measures that were employed with Li's and Brink's methods are listed in the tables. Moreover, results for both techniques' supervised performance metrics are displayed.

In conclusion, the outcomes of using the EPSM and PPSM models on various datasets are illustrated in these tables. They also offer further details regarding the distribution combinations and performance indicators that were applied in both methods.

Table 4. Examples of results from using EPSM and PPSM on the HAM10000 dataset

Image	Thresh. (Li)	Thresh. (Br)	Distr. (Li)	Distr. (Br)	(UN + RC)/2 (Li)	(UN + RC)/2 (Br)	(JI + DI + F-Score)/3 (Li)	(JI + DI + F-Score)/3 (Br)
ISIC_0024309	103	117	Gamma-Gaussian	Gaussian	0.376	0.358	0.482	0.648
ISIC_0024311	127	147	Gamma-Gaussian	Gaussian	0.368	0.353	0.610	0.824
ISIC_0024312	121	155	Gamma-Gaussian	Gamma-Gaussian	0.363	0.300	0.067	0.526
ISIC_0024313	109	124	Lognormal-Gaussian	Gaussian-Gamma	0.506	0.492	0.466	0.505
ISIC_0024314	121	141	Lognormal-Gaussian	Gamma	0.411	0.365	0.256	0.379
ISIC_0024315	94	106	Lognormal-Gaussian	Gaussian-Gamma	0.448	0.429	0.614	0.624

(Continued)

Table 4. Examples of results from using EPSM and PPSM on the HAM10000 dataset *(Continued)*

Image	Thresh. (Li)	Thresh. (Br)	Distr. (Li)	Distr. (Br)	(UN + RC)/2 (Li)	(UN + RC)/2 (Br)	(JI + DI + F-Score)/3 (Li)	(JI + DI + F-Score)/3 (Br)
ISIC_0024316	109	137	Gamma-Gaussian	Gaussian	0.348	0.335	0.000	0.002
ISIC_0024317	110	138	Lognormal-Gamma	Gaussian-Gamma	0.435	0.424	0.000	0.00006
ISIC_0024318	122	152	Gamma-Gaussian	Gamma-Gaussian	0.350	0.330	0.001	0.128
ISIC_0024782	119	147	Gamma-Gaussian	Gamma-Gaussian	0.382	0.323	0.458	0.393

Table 5. Examples of results from using EPSM and PPSM on the ISIC 2017 dataset

Image	Thresh. (Li)	Thresh. (Br)	Distr. (Li)	Distr. (Br)	(UN + RC)/2 (Li)	(UN + RC)/2 (Br)	(JI + DI + F-Score)/3 (Li)	(JI + DI + F-Score)/3 (Br)
ISIC_0000000	81	119	Lognormal-Gamma	Gamma	0.519	0.496	0.686	0.864
ISIC_0000001	88	102	Lognormal-Gaussian	Gaussian-Gamma	0.526	0.510	0.870	0.935
ISIC_0000002	34	126	Lognormal-Gamma	Gaussian-Gamma	0.674	0.402	0.000013	0.647
ISIC_0000007	33	101	Lognormal-Gamma	Gaussian-Gamma	0.676	0.471	0.002	0.507
ISIC_0000008	117	143	Lognormal-Gamma	Gaussian-Gamma	0.440	0.423	0.709	0.869
ISIC_0000009	115	130	Lognormal-Gamma	Gaussian-Gamma	0.407	0.391	0.680	0.792
ISIC_0000010	108	118	Lognormal-Gaussian	Gaussian-Gamma	0.413	0.397	0.677	0.736
ISIC_0000382	197	130	Gaussian-Gamma	Gamma-Gaussian	0.375	0.301	0.374	0.101
ISIC_0000384	109	133	Gamma-Gaussian	Gamma-Gaussian	0.384	0.325	0.519	0.361
ISIC_0000386	120	136	Gamma-Gaussian	Gaussian-Gamma	0.387	0.362	0.619	0.616

Samples of MRI images from the benchmark datasets utilized in this research are displayed in Figure 5. In the first column, the dataset's original image is shown. The second column shows the annotated image, and the third column shows the segmented image created by applying the EPSM code to the original image. The final column displays the histogram image and the optimal threshold value generated by this model.

Table 6. Examples of results from using EPSM and PPSM on the PH2 dataset

Image	Thresh. (Li)	Thresh. (Br)	Distr. (Li)	Distr. (Br)	(UN + RC)/2 (Li)	(UN + RC)/2 (Br)	(JI + DI + F-Score)/3 (Li)	(JI + DI + F-Score)/3 (Br)
IMD010	89	103	Lognormal-Gaussian	Gamma	0.487	0.460	0.003	0.009
IMD013	115	146	Lognormal-Gaussian	Gaussian	0.420	0.354	0.061	0.611
IMD006	114	131	Lognormal-Gaussian	Gaussian-Gamma	0.420	0.387	0.118	0.311
IMD008	128	145	Lognormal-Gaussian	Gaussian-Gamma	0.436	0.412	0.114	0.203
IMD023	101	133	Lognormal-Gaussian	Gaussian	0.442	0.353	0.013	0.188
IMD035	115	130	Lognormal-Gaussian	Gamma	0.473	0.455	0.000	0.002
IMD045	99	112	Lognormal-Gaussian	Gaussian-Gamma	0.481	0.466	0.001	0.004
IMD107	111	145	Lognormal-Gaussian	Gaussian-Gamma	0.477	0.398	0.013	0.331
IMD015	117	135	Lognormal-Gamma	Gaussian-Gamma	0.427	0.419	0.819	0.817
IMD031	139	138	Gamma-Gaussian	Gaussian	0.419	0.419	0.934	0.932

Table 7 results highlight the comparison between the EPSM approach and the U-Net model across three datasets: HAM10000, ISIC 2017, and PH2. For the HAM10000 dataset, the EPSM approach achieved high-performance results for 425 out of 500 images

(85%), significantly outperforming U-Net, which achieved high-performance results for only 75 images (15%). On the ISIC 2017 dataset, both methods performed similarly, with the EPSM approach achieving high-performance results for 252 images (50.4%) and U-Net for 248 images (49.6%). In contrast, for the PH2 dataset, U-Net demonstrated better performance with high-performance results for 126 images (63%), compared to EPSM approach which achieved high-performance results for 74 images (37%). From the results, it is evident that for high-quality images, such as those in the PH2 dataset, the U-Net approach outperforms the EPSM method. However, for other datasets, the EPSM approach shows better performance.

Table 7. The comparison of applying the EPSM and U-NET on the same datasets

Dataset	EPSM Approach	U-Net Model
HAM10000	425 (85%)	75 (15%)
ISIC 2017	252 (50.4%)	248 (49.6%)
PH2	74 (37%)	126 (63%)

4.2 Parallel processing efficiency

Finding the optimal threshold value t^* can be a computationally demanding operation when working with a dataset that contains a lot of images or numerous small images. The performance of the EPSM approach can be enhanced by combining MCET calculation and parallel processing technology to get around this problem. The computation time can be drastically decreased by making use of the parallel processing capacity of CPUs, enabling more effective processing of big datasets. This method can shorten the thresholding procedure and use less time and computing power while improving the accuracy of the segmentation results.

Healthcare applications, especially those related to the Internet of Medical Things (IoMT), can be greatly impacted by using parallel processing techniques to determine threshold values for medical image segmentation. Through sensors, cameras, and other internet-connected medical devices, the IoMT generates a large amount of data and images. Breast cancer, brain cancer, skin cancer, and other diseases are addressed by a number of real-time, automated medical classification systems that are based on Internet of Things infrastructure. Data latency, however, presents a significant problem for smart devices and apps that rely on real-time processing [44].

In the format of hh:mm:ss, Table 8 shows the amount of time needed to run the proposed MCET approach sequentially and using parallel techniques on the three benchmark datasets. The savings in speed that can be achieved through parallel processing are displayed in the table.

The parallel processing methods produced a speedup saving of about 43.67% for the PH2 dataset. Similar to this, the ISIC 2017 dataset saw a speedup saving of 39.83% because to the parallel processing technique. A speedup advantage of 47.25% was made possible by leveraging parallel processing to run the proposed model on the last dataset.

Table 8. Speedup saving when utilizing parallel computing techniques

Dataset	Sequential Time [hh:mm:ss]	Parallel Time [hh:mm:ss]	Speedup Saving Percentage
PH2	00:38:30	00:21:41	43.67%
ISIC 2017	08:13:17	04:56:48	39.83%
HAM10000	01:04:26	00:33:59	47.25%

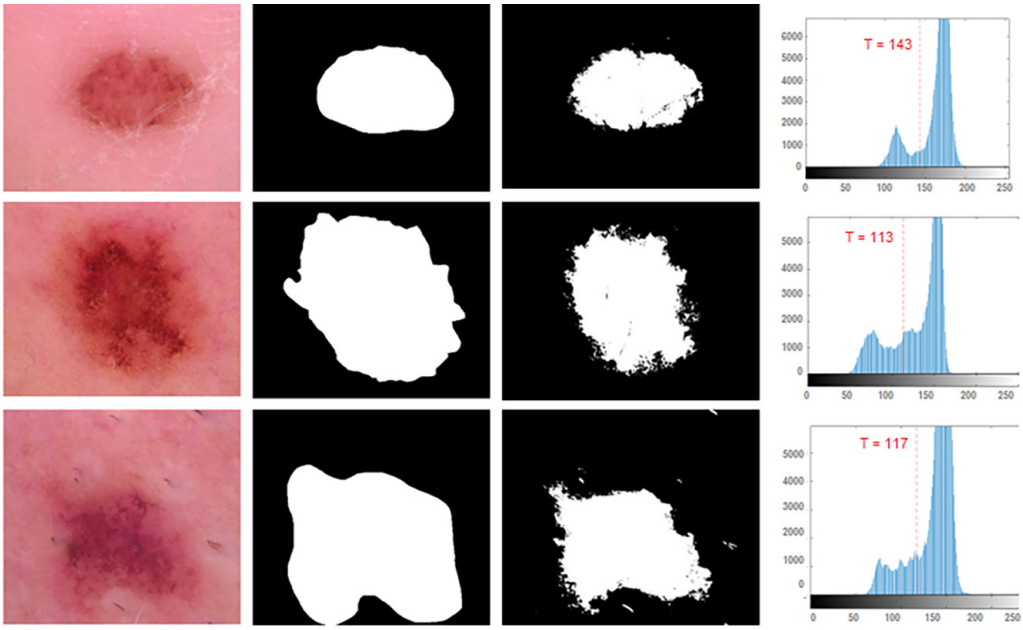

Fig. 5. Original image in column 1, annotated image in column 2, a segmented image produced by the EPSM algorithm in column 3, and the histogram image with the ideal threshold t* in the last column

The three datasets' combined average speedup increase was roughly 43.58%. Our findings show that adopting parallel processing techniques for the MCET approach in the EPSM model on large datasets might result in significant time savings. The Wilcoxon test was employed to assess the accuracy of the approach results, and the results revealed a considerable improvement when employing the parallel approach as opposed to the sequential strategy. The parallel approach's performance improvement is statistically significant, according to the test's p-value of 0.006317, which was obtained.

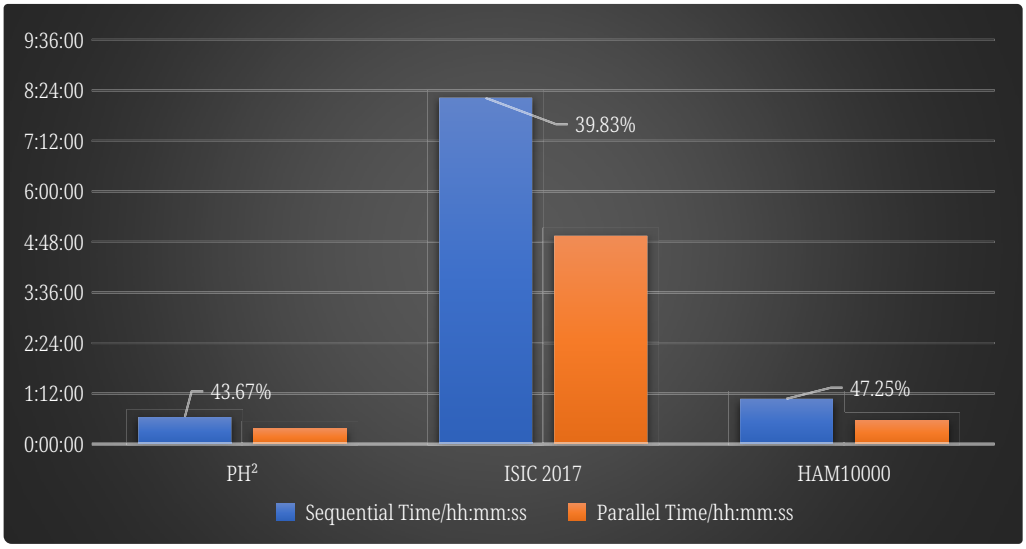

Fig. 6. Speedup saving

In a column-based graph, Figure 6 shows the time required to execute the suggested MCET strategy sequentially and in parallel on the three datasets.

5 CONCLUSIONS

This paper presents a novel thresholding method based on MCET that can be used to precisely segment medical images. The PH2, HAM10000, and ISIC 2017 datasets were used to test the proposed bimodal approach. Three alternative combinations of statistical distributions, namely Gaussian, Gamma, and Lognormal, were used to calculate the MCET of each input image. This method's main goal is to increase segmentation accuracy by optimizing both supervised and unsupervised performance metrics. The proposed method's outcomes were compared with those of Li's method. A novel parallel boosting segmentation technique was developed and put into use to further improve the performance of the EPSM model. This algorithm has been demonstrated to increase the effectiveness of the thresholding procedure, producing results in segmentation that are more precise.

Future work will focus on using sophisticated mathematical methods to speed up the proposed model's processing. This will improve the model's effectiveness and speed up the processing of massive datasets.

Funding: This research received no external funding.

Data availability statement: The data presented in this study are available upon request.

Conflicts of interest: The authors declare no conflict of interest.

6 REFERENCES

[1] W. K. Pratt, *Introduction to Digital Image Processing*. Boca Raton, FL: CRC press, 2013. https://doi.org/10.1201/b15731

[2] M. Heidari *et al.*, "Hiformer: Hierarchical multi-scale representations using transformers for medical image segmentation," in *Proceedings of the IEEE/CVF Winter Conference on Applications of Computer Vision (WACV)*, Waikoloa, HI, USA, 2023, pp. 6202–6212. https://doi.org/10.1109/WACV56688.2023.00614

[3] L. Abualigah, N. K. Al-Okbi, M. A. Elaziz, and E. H. Houssein, "Boosting marine predators algorithm by Salp Swarm algorithm for multilevel thresholding image segmentation," *Multimedia Tools and Applications*, vol. 81, pp. 16707–16742, 2022. https://doi.org/10.1007/s11042-022-12001-3

[4] E. H. Houssein, N. Abdalkarim, K. Hussain, and E. Mohamed, "Accurate multilevel thresholding image segmentation via oppositional Snake optimization algorithm: Real cases with liver disease," *Computers in Biology and Medicine*, vol. 169, p. 107922, 2024. https://doi.org/10.1016/j.compbiomed.2024.107922

[5] C. H. Li and C. Lee, "Minimum cross entropy thresholding," *Pattern Recognition*, vol. 26, no. 4, pp. 617–625, 1993. https://doi.org/10.1016/0031-3203(93)90115-D

[6] L. Zhao, S. Zheng, W. Yang, H. Wei, and X. Huang, "An image thresholding approach based on Gaussian mixture model," *Pattern Analysis and Applications*, vol. 22, pp. 75–88, 2019. https://doi.org/10.1007/s10044-018-00769-w

[7] B. Shah and R. Daniel, "Tsallis entropic thresholding based segmentation of Gas Puff images of plasma using normalize grey level spatial correlation histogram," in *2020 International Conference on Artificial Intelligence and Signal Processing (AISP)*, Amaravati, India, 2020, pp. 1–6. https://doi.org/10.1109/AISP48273.2020.9072966

[8] T. Pun, "A new method for grey-level picture thresholding using the entropy of the histogram," *Signal Processing*, vol. 2, no. 3, pp. 223–237, 1980. https://doi.org/10.1016/0165-1684(80)90020-1

[9] J. N. Kapur, P. K. Sahoo, and A. K. Wong, "A new method for gray-level picture thresholding using the entropy of the histogram," *Computer Vision, Graphics, and Image Processing*, vol. 29, no. 3, pp. 273–285, 1985. https://doi.org/10.1016/0734-189X(85)90125-2

[10] A. D. Brink and N. E. Pendock, "Minimum cross-entropy threshold selection," *Pattern Recognition*, vol. 29, no. 1, pp. 179–188, 1996. https://doi.org/10.1016/0031-3203(95)00066-6

[11] R. Chakraborty, R. Sushil, and M. L. Garg, "An improved PSO-based multilevel image segmentation technique using minimum cross-entropy thresholding," *Arabian Journal for Science and Engineering*, vol. 44, pp. 3005–3020, 2019. https://doi.org/10.1007/s13369-018-3400-2

[12] S. Rawas and A. El-Zaart, "Precise and parallel segmentation model (PPSM) via MCET using hybrid distributions," *Applied Computing and Informatics*, vol. 20, nos. 3/4, pp. 262–278, 2020. https://doi.org/10.1108/ACI-11-2020-0123

[13] M. T. Nyo, F. Mebarek-Oudina, S. S. Hlaing, and N. A. Khan, "Otsu's thresholding technique for MRI image brain tumor segmentation," *Multimedia Tools and Applications*, vol. 81, pp. 43837–43849, 2022. https://doi.org/10.1007/s11042-022-13215-1

[14] Z. Wang, F. Yu, D. Wang, and R. Hu, "Multi-threshold segmentation of breast cancer images based on improved dandelion optimization algorithm," *The Journal of Supercomputing*, pp. 1–25, 2023. https://doi.org/10.21203/rs.3.rs-3129915/v1

[15] J. Ramya, H. Vijaylakshmi, and H. M. Saifuddin, "Segmentation of skin lesion images using discrete wavelet transform," *Biomedical Signal Processing and Control*, vol. 69, p. 102839, 2021. https://doi.org/10.1016/j.bspc.2021.102839

[16] W. A. H. Jumiawi and A. El-Zaart, "Improvement in the between-class variance based on lognormal distribution for accurate image segmentation," *Entropy*, vol. 24, no. 9, p. 1204, 2022. https://doi.org/10.3390/e24091204

[17] N. R. Pal, "On minimum cross-entropy thresholding," *Pattern Recognition*, vol. 29, no. 4, pp. 575–580, 1996. https://doi.org/10.1016/0031-3203(95)00111-5

[18] N. A. Zreika, A. El Zaart, A. El Chakik, and T. El Arwadi, "Skin cancer segmentation with entropy PAL MCET using Gaussian distribution," in *2018 4th International Conference on Applied and Theoretical Computing and Communication Technology (iCATccT)*, Mangalore, India, 2018, pp. 315–320. https://doi.org/10.1109/iCATccT44854.2018.9001993

[19] N. Zreika, A. El-Zaart, and A. El Chakik, "A hybrid cross entropy thresholding for early Alzheimer's disease detection," *International Journal of Computing and Digital System*, 2021. https://doi.org/10.12785/ijcds/120161

[20] S. Rawas and A. El-Zaart, "HCET-G 2: Dermoscopic skin lesion segmentation via hybrid cross entropy thresholding using Gaussian and Gamma distributions," in *2019 Third International Conference on Intelligent Computing in Data Sciences (ICDS)*, Marrakech, Morocco, 2019, pp. 1–7. https://doi.org/10.1109/ICDS47004.2019.8942339

[21] W. A. H. Jumiawi and A. El-Zaart, "Gumbel (EVI)-based minimum cross-entropy thresholding for the segmentation of images with skewed histograms," *Applied System Innovation*, vol. 6, no. 5, p. 87, 2023. https://doi.org/10.3390/asi6050087

[22] A. Farahani and H. Mohseni, "Medical image segmentation using customized U-Net with adaptive activation functions," *Neural Computing and Applications*, vol. 33, pp. 6307–6323, 2021. https://doi.org/10.1007/s00521-020-05396-3

[23] Y. Yang, C. Feng, and R. Wang, "Automatic segmentation model combining U-Net and level set method for medical images," *Expert Systems with Applications*, vol. 153, p. 113419, 2020. https://doi.org/10.1016/j.eswa.2020.113419

[24] S. Rahimi, M. Zargham, A. Thakre, and D. Chhillar, "A parallel Fuzzy C-Mean algorithm for image segmentation," in *IEEE Annual Meeting of the Fuzzy Information, 2004. Processing NAFIPS '04*, Banff, AB, Canada, vol. 1, 2004, pp. 234–237. https://doi.org/10.1109/NAFIPS.2004.1336283

[25] M. Al-Ayyoub, A. M. Abu-Dalo, Y. Jararweh, M. Jarrah, and M. A. Sa'd, "A GPU-based implementations of the fuzzy C-means algorithms for medical image segmentation," *The Journal of Supercomputing*, vol. 71, pp. 3149–3162, 2015. https://doi.org/10.1007/s11227-015-1431-y

[26] A. Prahara, A. Pranolo, N. Anwar, and Y. Mao, "Parallel approach of adaptive image thresholding algorithm on GPU," *Knowledge Engineering and Data Science*, vol. 4, no. 2, pp. 69–84, 2022. https://doi.org/10.17977/um018v4i22021p69-84

[27] M. N. Akhtar, J. M. Saleh, H. Awais, and E. A. Bakar, "Map-reduce based tipping point scheduler for parallel image processing," *Expert Systems with Applications*, vol. 139, p. 112848, 2020. https://doi.org/10.1016/j.eswa.2019.112848

[28] T. Mendonça, M. Celebi, T. Mendonca, and J. Marques, "Ph2: A public database for the analysis of dermoscopic images," *Dermoscopy Image Analysis*, 2015.

[29] N. C. Codella *et al*., "Skin lesion analysis toward melanoma detection: A challenge at the 2017 international symposium on biomedical imaging (ISBI), hosted by the international skin imaging collaboration (ISIC)," in *2018 IEEE 15th International Symposium on Biomedical Imaging (ISBI 2018)*, Washington, DC, USA, 2018, pp. 168–172. https://doi.org/10.1109/ISBI.2018.8363547

[30] P. Tschandl, C. Rosendahl, and H. Kittler, "The HAM10000 dataset, a large collection of multi-source dermatoscopic images of common pigmented skin lesions," *Scientific Data*, vol. 5, pp. 1–9, 2018. https://doi.org/10.1038/sdata.2018.161

[31] A. Hati, R. Velmurugan, S. Banerjee, and S. Chaudhuri, *Image Co-Segmentation*. Singapore: Springer Nature, 2023. https://doi.org/10.1007/978-981-19-8570-6

[32] F. Nie, P. Zhang, J. Li, and D. Ding, "A novel generalized entropy and its application in image thresholding," *Signal Processing*, vol. 134, pp. 23–34, 2017. https://doi.org/10.1016/j.sigpro.2016.11.004

[33] S. Kullback, *Information Theory and Statistics*. Boston, MA: Courier Corporation, 1997.

[34] A. Al-Ajlan and A. El-Zaart, "Image segmentation using minimum cross-entropy thresholding," in *2009 IEEE International Conference on Systems, Man and Cybernetics*, San Antonio, TX, USA, 2009, pp. 1776–1781. https://doi.org/10.1109/ICSMC.2009.5346619

[35] A. El-Zaart, "Synthetic aperture radar images segmentation using minimum cross entropy with Gamma distribution," *International Journal of Signal and Image Processing*, vol. 6, no. 4, pp. 19–31, 2015. https://doi.org/10.5121/sipij.2015.6402

[36] N. Zreika, A. Zreika, N. Aref, A. El Zaart, and A. Al Shakik, "An improvement of cross entropy thresholding for skin cancer," *BAU Journal-Science and Technology*, vol. 2, no. 2, p. 2, 2021.

[37] H. Zhang, J. E. Fritts, and S. A. Goldman, "Image segmentation evaluation: A survey of unsupervised methods," *Computer Vision and Image Understanding*, vol. 110, no. 2, pp. 260–280, 2008. https://doi.org/10.1016/j.cviu.2007.08.003

[38] C.-I. Chang, Y. Du, J. Wang, S.-M. Guo, and P. Thouin, "Survey and comparative analysis of entropy and relative entropy thresholding techniques," *IEE Proceedings-Vision, Image and Signal Processing*, vol. 153, no. 6, pp. 837–850, 2006. https://doi.org/10.1049/ip-vis:20050032

[39] W. A. H. Jumiawi and A. El-Zaart, "Improving minimum cross-entropy thresholding for segmentation of infected foregrounds in medical images based on mean filters approaches," *Contrast Media & Molecular Imaging*, vol. 2022, no. 1, pp. 1–14, 2022. https://doi.org/10.1155/2022/9289574

[40] S. Azmat, L. Wills, and S. Wills, "Parallelizing multimodal background modeling on a low-power integrated GPU," *Journal of Signal Processing Systems*, vol. 88, pp. 43–53, 2017. https://doi.org/10.1007/s11265-016-1111-z

[41] N. Siddique, S. Paheding, C. P. Elkin, and V. Devabhaktuni, "U-Net and its variants for medical image segmentation: A review of theory and applications," *IEEE Access*, vol. 9, pp. 82031–82057, 2021. https://doi.org/10.1109/ACCESS.2021.3086020

[42] P. S. Xavier, P. K. Sathish, and G. Ragu, "Advancing brain tumor segmentation in MRI scans: Hybrid attention-residual UNET with transformer blocks," *International Journal of Online & Biomedical Engineering (iJOE)*, vol. 20, no. 6, pp. 103–115, 2024. https://doi.org/10.3991/ijoe.v20i06.46979

[43] S. Rawas and A. D. Samala, "Revolutionizing brain tumor analysis: A fusion of ChatGPT and multi-modal CNN for unprecedented precision," *International Journal of Online & Biomedical Engineering (iJOE)*, vol. 20, no. 8, pp. 37–48, 2024. https://doi.org/10.3991/ijoe.v20i08.47347

[44] I. Dhaini, S. Rawas, and A. El-Zaart, "An intelligent and green E-healthcare model for an early diagnosis of medical images as an IoMT application," in *Distributed Computing and Artificial Intelligence, Special Sessions, 19th International Conference, DCAI 2022*, *Lecture Notes in Networks and Systems*, J. M. Machado *et al.*, Eds., Springer, Cham, vol. 585, 2022, pp. 159–164. https://doi.org/10.1007/978-3-031-23210-7_16

7 AUTHORS

Ibrahim N. Dhaini, currently a Ph.D. candidate, holds a master's and bachelor's degree in computer science from the Lebanese American University (LAU). He is presently engaged in his doctoral studies in computer science at Beirut Arab University. Ibrahim specializes in medical image processing, the Internet of Medical Things (IOMT), and cloud computing (E-mail: ind301@student.bau.edu.lb).

Ali El-Zaart was promoted to full professor rank in computer science in March 2016. He received a M.Sc. (1996) and Ph.D. (2001) degrees in computer science from the University of Sherbrooke, Sherbrooke, Quebec, Canada. Since 2011, he has been a faculty member at Beirut Arab University (BAU). He has published numerous (more than 160) articles and proceedings in the area of smart sustainable cities, image processing, data mining, machine learning, cloud computing (E-mail: elzaart@bau.edu.lb).

Soha Rawas holding a Ph.D. in Mathematics and Computer Science, graduated from Beirut Arab University (BAU) in 2019. Dr. Rawas possesses a broad spectrum of expertise spanning several domains, notably artificial intelligence, deep learning, the Internet of Medical Things (IOMT), cloud computing, and image processing. With unwavering dedication to her research pursuits, she currently serves as an academic lecturer within the Faculty of Science, Department of Mathematics and Computer Science, at Beirut Arab University (BAU). In addition, she holds a managerial role at the Continuing Education Center (CEC) at BAU (E-mail: soha.rawas2@bau.edu.lb).